A New Strategy of 3D Printing Lightweight Lamellar Graphene Aerogels for Electromagnetic Interference Shielding and Piezoresistive Sensor Applications

*Hao Guo, Tianxiang Hua, Jing Qin, Qixin Wu, Rui Wang, Bo Qian *, Lingying Li and Xuejun Shi*

Hao Guo, Rui Wang, Bo Qian, Lingying Li

Suzhou Institute of Nano-Tech and Nano-Bionics, Chinese Academy of Sciences, Suzhou 215123, China;

E-mail: bqian2010@sinano.ac.cn

Tianxiang Hua, Jing Qin, Qixin Wu,

School of Nano Technology and Nano Bionics, University of Science and Technology of China, Suzhou 215123, China;

Xuejun Shi

School of Physical Science and Technology, Soochow University, Suzhou 215031, China;

Keywords: lamellar graphene aerogel; 3D printing; graphene oxide liquid crystal; electromagnetic interference shielding; piezoelectric sensor

Abstract

Lamellar 3D structures are beneficial to raise the electrical properties of graphene aerogels like electrical conductivity, electromagnetic interference (EMI) shielding efficiency (SE) and pressure sensitivity. In this paper, we demonstrate a strategy of 3D printing lamellar graphene aerogel (LGA) based on shear-thinning and ice-growth-inhibition mechanisms. A well-designed slit extrusion printhead was used to produce shear thinning graphene oxide (GO) water-based dispersions. Tert-butyl alcohol (TBA) was added into GO water-based dispersions to inhibit ice growth which will destroy the GO flakes arrangement. After freeze-drying and chemical reduction of the printed GO samples, the lightweight LGAs were prepared. Comparing to the traditional way, the strategy in this paper shows much better size and shape scalable freedom. The LGA exhibit electrical conductivity up to 705.6 S m^{-1}, which is rather

high for graphene-based aerogels. Benefiting from the lamellar structure and high electrical conductivity, the aerogel achieves up to 68.75 dB EMI SE at X-band with the thickness of 3 mm, while the absolute EMI SE can reach up to 15351.9 dB $cm^3 g^{-1}$. The LGA can also be used as a piezoelectric pressure sensor, which exhibits high compressible stress and rapid response time.

1. Introduction

Ultra-low density 2D material-based aerogels enable various applications, such as sensors,[1] electromagnetic shielding,[2] flexible devices,[3] supercapacitors,[4] and oil absorption.[5] Since 2D materials have lamellar atoms' arrangement, 2D materials-based aerogels with lamellar arrangement possess different properties along different directions. In certain direction, the lamellar 2D materials-based aerogels show much better mechanical, electrical, and thermal properties than the isotropic ones.[6]

Since the first discovery of graphene,[7] how to assemble graphene nanosheets conveniently in an ordered way is quite important for the real industry application.[8] At present, the directional freezing casting method is commonly employed to prepare anisotropic aerogels, the principle of which is to employ anisotropic temperature gradient to control the direction of ice crystal formation.[9] During the freeze crystallization process, the solvent first crystallizes into nuclei near the surface of the low temperature, and then grows in the direction of temperature gradient to form ordered ice crystals and squeeze the solute between the ice crystals. Subsequently, anisotropic aerogels were obtained by vacuum drying.[10] Several ways such as unidirectional freezing[11], bidirectional freezing[12], and radial freezing[13] have been successfully applied to control the porosity and microstructure of aerogels. Bidirectional freezing, in particular, has been successfully applied and used to prepare layered aerogel structures. This method is achieved by controlling the nucleation and growth of ice crystals by generating a double temperature gradient using insulated media such as PDMS in a container. At present, lamellar aerogels prepared by bidirectional freezing method have been successfully used for multiple applications such as thermal interface composites[14], piezoresistive sensors[6c, 15], electromagnetic shielding[16], oil absorption[17], and so on. However, due to the restrictions on mold shape and the ice growth direction perpendicular to the freezing substrate, this method

is difficult to prepare graphene aerogels with more degrees of freedom in size and shape which limits their potential applications in industry. [10, 18]

On the other hand, the graphene oxide (GO) dispersions have been observed shear thinning behavior, which transfers the GO dispersions from a colloidal isotropic state to nematic liquid crystal (LC) phase when the GO sheets in dispersions reach to a critical concentration according to the Onsager theory.[19], [20] This characteristic of the graphene oxide liquid crystals (GOLCs) has been widely used in wet spinning[21] and DIW(Direct Ink Writing, which is an extrusion-based additive manufacturing method)[22]. The question is how to achieve large area parallel arrangement of 2D materials after the freeze-drying aerogels formation process, since the ice growth directional property could destroy the orientation structure.[23] Previous studies demonstrated that tert-butyl alcohol (TBA) can form small eutectic with water during freeze-drying, which effectively prevents the growth of micron-scale ice crystal.[24] This may be the solution for the question proposed above.

In this paper, we study and demonstrate a 3D printing lamellar graphene aerogels method based on shear-thinning and ice-growth-inhibition mechanisms. Firstly, to prepare large-area ordered GOLCs, we replaced the DIW needle head of a syringe by a slit extrusion head. To perform shear stress on different GO dispersions effectively, the slit extrusion heads were carefully designed through the coat-hanger die design equations.[25] Then the slit extrusion heads for the different GO dispersions were prepared by projection microstereolithography. Secondly, GO dispersions with different mass fractions of TBA, were 3D printed layer by layer through the specific designed slit extrusion heads on freezing substrate. Finally, after freeze-drying and chemical reduction of the printed samples, the graphene aerogels were prepared. With the mass fraction of TBA increasing, the arrangement of the sheets in the graphene aerogels changed from perpendicular to parallel to the substrate. The LGA sample shows the best electrical conductivity of 705.6 S m^{-1} and EMI SE of 68.75 dB at X-band for 3 mm sample, which are at a high level comparing to the reported values of graphene-based aerogels. Furthermore, the LGA also exhibits piezoresistive performance including high compressible stress of 166.51 kPa at 80% strain and rapid response of 32 ms (at 20% strain). In addition, the method in this paper shows size and shape scalable freedom, and can be widely used for all the 2D material dispersions with shear thinning behavior to prepare lamellar aerogels, and explore

the possibility of the property improvement of 2D material-based aerogels.

2. Results and Discussion

The idea of the 3D printing LGA based on shear-thinning and ice-growth-inhibition mechanisms is depicted in the schematics in Figure 1. First, three GO aqueous dispersions with TBA mass fraction of 0%, 20%, and 40% were prepared, marked as GO-T0, GO-T2, and GO-T4, respectively. Then, one of the three GO dispersions was poured into a syringe mounted with a slit extrusion head, which was designed according to the rheological properties of this GO dispersion. By controlling the air pressure in the syringe, the GO dispersions were printed with strong shear stress from the flow channel, and became GOLCs with long-range highly ordered sheets based on shear thinning mechanism. After layer-by-layer printed on freezing substrate, for the GO dispersions with optimum mass fraction of TBA, it is supposed that the GOLCs orientation can be maintained after freezing, and lamellar GO aerogel can be prepared after freeze-drying of the printed sample. Then the LGA can be prepared after chemical reduction of the lamellar GO aerogel. the GO aerogels are named as GOA-T0, GOA-T2, and GOA-T4, while the graphene aerogels after reducing the GO aerogels are named as GA-T0, GA-T2, and GA-T4.

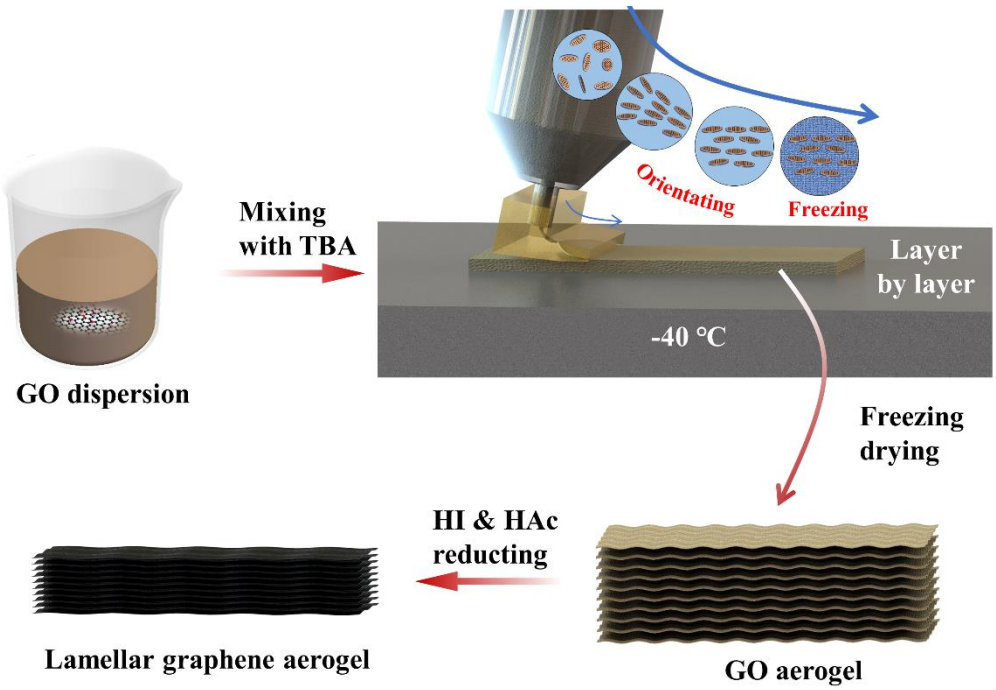

Figure 1. Schematic of 3D printing LGA process. GO dispersions mixed with TBA was printed layer by layer on the freezing substrate at -40 °C through the designed extrusion head. With the

optimum mass fraction of TBA, GO dispersion sequentially becomes aligned graphene oxide liquid crystals (GOLCs) under shear stress, lamellar GO aerogel after freeze-drying, and LGA after reduction by hydroiodic acid and acetic acid.

2.1. Design and preparation of slit extrusion head

In Figure 2a, for all the three dispersions, the shear viscosity decreases rapidly when the shear rate increases from 0.1 s^{-1} to 10000 s^{-1}. The viscosity rapid decreasing behavior of the three dispersions means that GO sheets are more and more parallel to the flow direction with the shear rate increasing. Such exponentially decreasing viscosity-shear rate relationships of the GO dispersions are consistent with the shear thinning characteristics of the typical pseudoplastic fluid[19b, 19e]. Note that with the TBA content increasing, the decreasing speed of the viscosity becomes slightly slower. The viscosity value sequence changes inversely from GO-T0>GO-T2>GO-T4 to GO-T0<GO-T2<GO-T4 at around the shear rate of 4 s^{-1}. Since the cooperative hydrogen-bond prefers to form between water and the GO sheets, at the low shear rate side, the fluid flow needs to overcome the large flow resistance from the electrostatic interaction between water and disordered GO sheets, the increasing of TBA content will decrease the flow resistance as well as the viscosity. On the contrary, at the high shear rate side, the shear thinning mechanism makes the GO sheets order, and the flow resistance becomes too low to have influence on the viscosity. In this case, the viscosity of the GO dispersions is close to the mixture of water and TBA without GO sheets. Figure 2b shows the elastic modulus (G') and viscous modulus (G") of the three GO dispersions as a function of shear stress. The G' and G" of all the three GO dispersions show decreasing curves with the shear stress increasing in the range from 0.02 Pa to 4 Pa. For each GO dispersion, G' is about one order of magnitude higher than G" at the low shear stress side, and decreases faster than G" with the shear stress increasing. When the shear stress increases over the cross point of G' and G", the GO dispersions turn to GOLCs with long-range ordered GO sheets, which means the GO dispersions lose most of the elastic properties and viscous modulus plays a dominant role in the dispersions. Note that the shear stress at the cross points and most values of the G' and G" are following a sequence of GO-T0<GO-T2<GO-T4, which indicates the addition of TBA in GO dispersions could increase the disorder degree of the water molecular and GO networks.

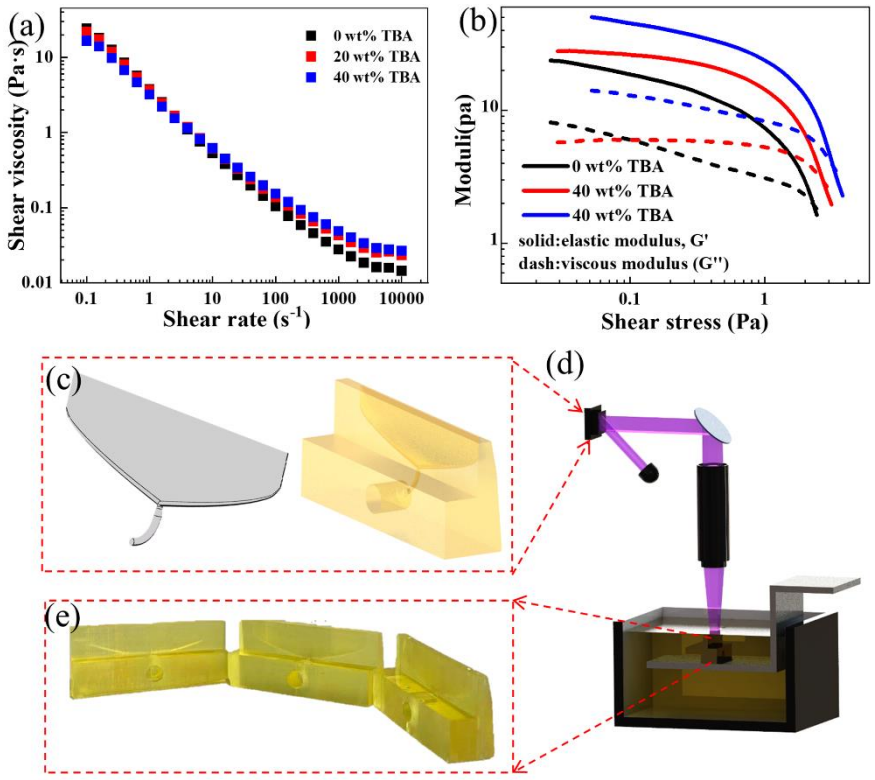

Figure 2. GO dispersions' rheological properties and slit extrusion head. (a) Apparent viscosity as a function of shear rate, and (b) elastic and viscous modulus as a function of shear stress of GO dispersions with different TBA content. (c) Designed inside fluid channel (left) and solid structure (right) of slit extrusion head. (d) Schematic of Projection microstereolithography 3D printing. (e) Three fabricated extrusion head for three GO dispersions, respectively.

Based on the rheological property, the slit extrusion head for each GO dispersion was designed as a coat-hanger die structure[26] as show in Figure 2c. The coat-hanger die is mainly divided into the inlet, manifold and sector slit area as shown in Figure S2. Fluid flows into the die through the inlet, evenly distributes to the entire sector through the manifold, gets greater shear stress in the sector, and finally flows out of the die. The coat-hanger die structure in the slit extrusion head was designed according to the power equation in Equation 1 which is a constitutive equation for non-Newtonian fluids.

$$\eta = K \cdot \gamma^{n-1} \tag{1}$$

Where η is the shear viscosity, γ is the shear rate, K is the consistency coefficient, and n is the viscosity index. Based on the viscosity-shear rate curves of GO-T0, GO-T2, and GO-T4 in Figure 2a, three groups of the power-law parameters of K and n were fitted by Equation (1) and

listed in Table S1, respectively.

The slit channel thickness is essential in the design parameters of the extrusion head. According to Figure 2a, the GO dispersions show typical pseudoplastic fluid behavior which is supposed to be plunger flow in the slit structure. Equation S4 and S5 present the shear rate and velocity of pseudoplastic fluid plunger flow in the slit, respectively. It can be noticed in Equation S5 that the shear stress is increasing from the center to the edge plane of the slit. Meanwhile, the shear stress of the fluid at the edge plane of the slit is inversely proportional to the square of slit channel thickness. It means that reducing the slit channel thickness would increase the shear stress of the flow at the edge plane as well as the flow at the center plane since the distance from center to edge would also reduce. Therefore, reducing the thickness of the slit is significantly important for the shear-induced orientation of GO dispersions. In this case, we designed the slit channel of each extrusion head with the thickness as thin as possible of only 50 μm, which was attributed to the high resolution (10 μm) of the projection microstereolithography 3D printer[27] in Figure 2d. The flow channel structure was designed according to the design equations of a coat-hanger die of Equation S1-S3, with the parameters listed in Table S1. The overall dimensions of each extrusion head are 35 mm × 15 mm × 10 mm as shown in Figure 2e and S3a-c, and the optical pictures of the slit outlet are shown in Figure S3d-e.

2.2. Preparation of large-area ordered graphene oxide liquid crystals

The fluid behavior of GO dispersions in the extrusion head were simulated. Figure 3a illustrates the velocity contour plots of the GO-T4 dispersions and the outlet velocity distribution at the center plane of the extrusion head. According to the velocity contour plots, at the center of the inlet, the dispersions mainly flow along x direction with a speed of about 360 mm s^{-1}. Then most of the dispersions flow into the manifold with the velocity gradually dropping from 360 mm s^{-1} to 100 mm s^{-1}. Finally, the dispersions flow into the sector area and be evenly distributed with the velocity suddenly dropping from 100 mm s^{-1} to 10s mm s^{-1}. According to the blue curve in Figure 3a, the velocity at the outlet ranges between 53 mm s^{-1} and 65 mm s^{-1} from center to edge. Figure 3b and 3c illustrate the velocity, shear rate and viscosity distributions of GO-T4 dispersion at the central cross section and its outlet of the sector area by contour plots and data curves, respectively. In Figure 3b, the distributions show uniform and symmetric

property in x and z directions, respectively. In Figure 3c, the distributions with the thickness changing at the outlet of the cross section show symmetric behavior with parabolic curve opening downward, parabolic curve opening upward, and Lorentzian curve for velocity, shear rate and viscosity, respectively. Note that there are oscillations on the shear rate and viscosity curves because data are unstructured. Generally, the three kinds of distributions are consistent to each other. The maximum velocity, minimum shear rate, and maximum shear viscosity are at the center of the cross section of 53 mm s^{-1}, 70 s^{-1}, 0.18 Pa s, respectively. The minimum velocity, maximum shear rate, and maximum shear viscosity are at the edge of the cross section of 0 mm s^{-1}, 4697 s^{-1}, and 0.03 Pa s, respectively. The velocity curve is flat with the thickness from 23 to 27 μm. That means there is only a little plunger flow at the center, which can be neglected. The minor change of viscosity from 0.03 Pa s to 0.18 Pa s shows obvious shear thinning behavior of the GO dispersions. Figure 3d shows the isobaric lines of GO-T4 dispersion in the flow channel. The pressure in the manifold decreases from 45 kPa at the inlet to 25 kPa at the end. The pressure in the sector slit gradually decreases from 45 kPa close to the inlet to 0 kPa at the outlet with the isobaric lines parallel to y axis and connected with the lines in the manifold. Such pressure distribution facilitates uniform flow velocity distribution in Figure 3a. The simulated velocity, shear rate and viscosity distributions of GO-T0 and GO-T2 dispersions are illustrated in Figure S4. It can be found that the velocity and shear rate distributions of the three GO dispersions in Figure S4a-c is quite close to each other. This is due to the strategy of one extrusion head for one GO dispersions reducing the differences between the rheological properties of the different dispersions.

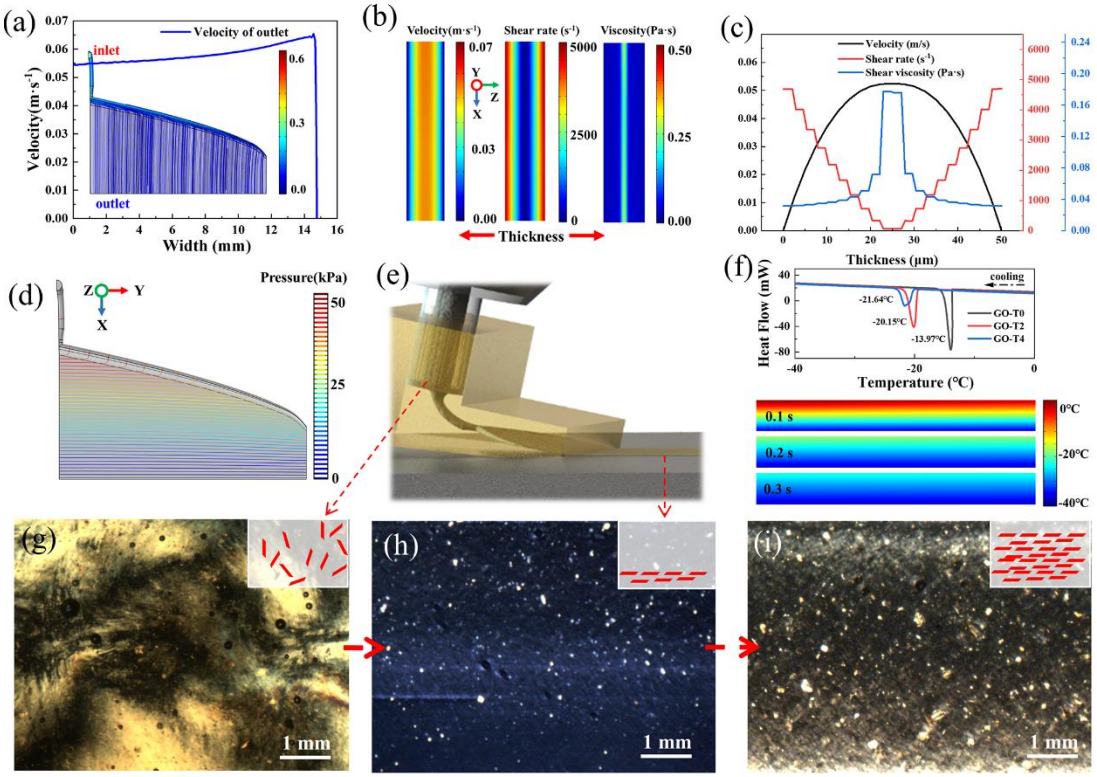

Figure 3. Simulation and experimental results of extrusion process. (a) Velocity contour plots of GO-T4 dispersion (inset) and outlet velocity distribution (blue curve) at the center plane of the extrusion head. Contour plots (b) and curves (c) of velocity, shear rate and viscosity of GO-T4 dispersion at the central cross section and its outlet at the sector area. (d) Pressure contour plots of GO-T4 dispersion at the center plane of the extrusion head. (e) Schematic diagram for illustrating the extrusion process. (f) Differential scanning calorimetry (DSC) curves of GO-T0, GO-T2 and GO-T4 dispersions and simulated time dependent temperature distributions of one layer GO-T4 dispersion after extrusion. Polarized optical microscope (POM) images of GO-T4 dispersion before extrusion (g), after one layer extrusion (h) and after multilayer extrusion (i), the scale bar represents 1 mm, the insets present the GO sheets arrangements. The red arrows represent the relationships between the pictures.

Figure 3e is the extrusion process schematic diagram drawn for the convenience of illustrating the GO sheets arrangements evolution after extrusion. Since the freezing process is very important for 3D printing and the formation of the final structure, the DSC curves from 0 °C to -40 °C of the three kinds of GO dispersions were measured and shown in the upper diagram in Figure 3f. It can be observed that with the TBA concentration increasing from GO-T0 to GO-T2, then to GO-T4, the freezing point decreases fast from -13.97 °C to -20.15 °C,

then slowly to -21.64 °C; The lower contour plots in Figure 3f show the simulation results of the time dependent temperature distributions of one layer GO-T4 dispersions after extrusion on the substrate. It can be observed that, at the initial, the upper and bottom surface temperatures of the one-layer dispersions are 0 °C and -40 °C, respectively. When the time reaches 0.3 s, the upper surface temperature drops to about -25 °C, which is lower than the freezing points of all the three kinds of GO dispersions. This (0.3s) is much shorter than the interval (about 5s) between the printed neighbor layers. Meanwhile, the simulated freezing time (6s) of 3mm GO dispersions in Figure S5 is also much shorter than the total printing time (300s) of 3mm sample. The simulated results indicate that each layer of the printed GO dispersions is well solidified before printing the next layer. Figure 3g-i are the polarized optical microscope (POM) images of GO-T4 at the different stages of the extrusion printing process at room temperature. Figure 3g shows the birefringent optical texture of GO dispersion before extrusion. It can be observed that the dark and bright patterns are randomly distributed on the substrate, which reflects the short-range order of the GO sheets. Figure 3h shows the POM image of the extruded single-layer GO dispersions. It is difficult to observe the birefringence phenomena due to the thin sample thickness of about 50 μm. Figure 3i shows the POM image of multilayer extruded GO dispersions. It can be observed there is a large area and homogeneous dark phase, which can be attributed that the GO dispersions becomes long range ordered GOLCs by extrusion process, and specifically, the GO sheets and the guided light propagation are parallel to the substrate.[28] The same phenomena of GO-T0 and GO-T2 dispersions can be found in Figure S6.

2.3. Preparation and characterization of GO aerogels and graphene aerogels

After extruding and freeze-drying, three kinds of GO aerogels (GOAs) were prepared. Figure 4a-c show the SEM images of GOA-T0, GOA-T2 and GOA-T4. In Figure 4a, it can be found that the arrangement of the GO sheets of GOA-T0 sample is shaped by the exclusion effect of the vertical growth of ice crystals, which totally loses the original horizontally oriented structure of GOLCs. Many large pores between GO sheets can be observed in Figure 4a, which indicates the large size of ice crystals. In Figure 4b, for GOA-T2, the pores between the GO sheets are much smaller than that in GOA-T0. There are no obvious vertical orientation structures, while some small lamellar structures close to parallel to the substrate can be found. In Figure 4c, the whole structure turns to be lamellar, with some small pores between the lamellar layers.

According to the TBA-H_2O phase diagram,[29] when the TBA concentration is in the range of 0–20 wt%, the solid phase consists of ice and TBA-H_2O eutectic; when the TBA concentration is in the range of 20–70 wt%, the solid phase consists of TBA hydrates and TBA-H_2O eutectic. Because of the small size of the needle-shaped TBA-H_2O eutectic crystals, the exclusion effect of crystals will be ineffective[24]. This can also be demonstrated in the DSC cooling curves (Figure 3f): The peak intensity decreases with the TBA concentration increasing, which means that the number of freezing crystals decreases greatly. The full-width at half maximum of the peaks also increases with the TBA concentration increasing, which indicates the freezing crystals become smaller and more disordered. Therefore, the TBA concentration dependent microstructure evolution behavior can be named as the ice-growth-inhibition mechanism. Additionally, all the three kinds of GOA exhibit ultralight properties, and GOA-T4 is shown in Figure 4d as an example, which can be easily held on the flower pistils. Figure 4e-g show the morphologies of the three kinds of GA reduced by the mixed solution of hydriodic acid (HI) and acetic acid (HAc).[30] It can be observed, compared with the corresponding GOAs in Figure 4a-c , the pore size of GAs in Figure 4e-g become larger and the graphene sheets arrangement become easier to distinguish. The pore size of GA-T0 is much larger than that of GA-T2 and GA-T4, and the graphene sheets alignment of GA-T0 is mainly vertical to the substrate. The pore size distribution of GA-T2 is close to be homogeneous with the lamellar structures in some small areas. For GA-T4, there are clear lamellar multi-arch structures. After the chemical reduction process, the graphene sheets were rearranged to the close packed lamellar sublayers which are connected to each other through many small pores with the size < 10 um. The close packed graphene sheets and small pores connection between the sublayers are beneficial to the electron transport properties; while the micro-arch structure of the wrinkled sublayers is beneficial to the compressive properties. In Figure 4h, GA-T4 exhibits good shape recovery property after compression. Generally, attributing to the ice-growth inhibition effect of TBA, GA-T4 inherits most long-range ordered structures from GOLCs, and remains lamellar, which is first demonstrated for DIW. More attractively, GA-T4 can be defined with any shape and size as shown in Figure S7, which will be applied in large area industry applications.

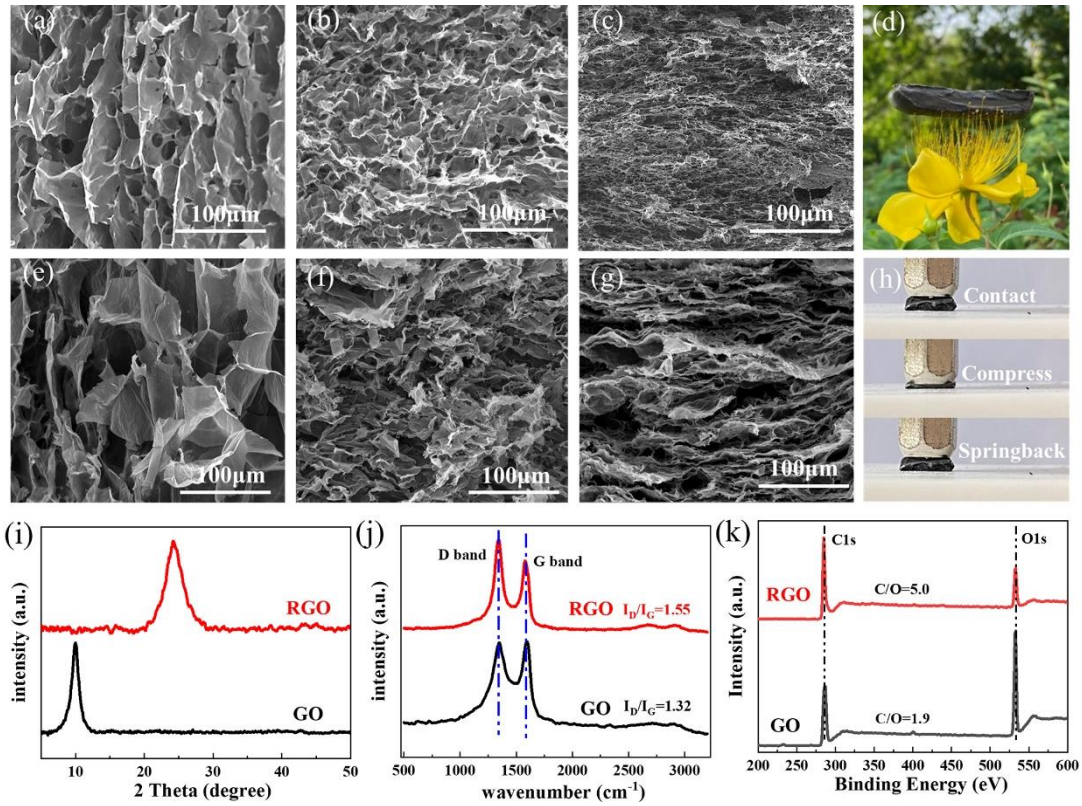

Figure 4. The structure properties of GOAs and GAs. Scanning electron microscopy (SEM) images of (a) GOA-T0, (b) GOA-T2, and (c) GOA-T4. (d) GOA-T4 on the flower pistils. SEM images of (e) GA-T0, (f) GA-T2 and (g) GA-T4. (h) Compression test processes of GA-T2. (i) X-ray diffraction (XRD) patterns, (j) Raman spectroscopy, and (k) X-ray photoelectron spectroscopy (XPS) of GOA-T4 and GA-T4.

The detail structure properties of GOA-T4 and GA-T4 were measured by X-ray diffraction (XRD), Raman spectroscopy and X-ray photoelectron spectroscopy (XPS), respectively. Figure 4i presents the XRD results. Characteristics of the carbon peak (001) for the GO sheets in GOA-T4 appeared at 10° corresponding to the definite d-spacing of 8.86 Å. After reduction, for GA-T4, (001) peak eventually disappears while the new peak (002) appears at 24.2°, which is corresponding to the graphene sheets d-spacing of 3.67 Å. This decrease of the d-spacing means the graphene sheets in the GA-T4 sublayers become more compact.[31] Figure 4j shows the micro-Raman spectra of GOA-T4 and GA-T4 to confirm the notable structural changes after chemical reduction. There are two main peaks of D and G for each sample. The D peaks of the two samples locate at the same position of 1343 cm^{-1}. The G peak shifts from 1595 cm^{-1} for GOA-T4 to 1579 cm^{-1} for GA-T4, corresponding to the recovery of the hexagonal network of

carbon atoms with defects. The D and G peak intensity ratios (I_D/I_G) are 1.32 for GOA-T4 and 1.55 for GA-T4, respectively. This increase confirms the reduction in average size of sp^2 domains and edge defects generation, which results from the removal of oxygen-containing functional groups from carbon skeleton.[32] Figure 4k presents the XPS spectra. Both GOA-T4 and GA-T4 show clear C 1s and O 1s peaks at around 286.0 eV and 533.0 eV. The peak intensity ratio of C/O increases from 1.9 for GOA-T4 to 5.0 for GA-T4, which indicates that most of the GO sheets have been reduced to graphene in GA-T4. In details, there are three deconvoluted C 1s peaks in Figure S10 at 284.8 eV, 286.9 eV and 288.6 eV, which are corresponding to unoxidized carbons (C-C/C=C), carbons in hydroxyl and epoxy groups (C-O), and carbonyl groups and carboxyl groups (C=O), respectively.[33] After GOA-T4 was reduced, the signal intensities of hydroxyl and epoxy decreased significantly as most of the oxygen-containing functional groups were removed, as shown in the green curve in Figure S10. In addition, C-C/C=C peak accounts for the majority of C 1s peak, which further confirms the ideal reduction results. [34]

2.4. Test and analysis of electromagnetic shielding performance

Figure 5a compares the in-plane electrical conductivities of the three kinds of GAs. The conductivity of GA-T0, GA-T2 and GA-T4 are 191.1 S m^{-1} 551.5 S m^{-1} and 705.6 S m^{-1}, respectively. The large increase of the in-plane electrical conductivity from GA-T0 to GA-T2, then to GA-T4 should be attributed to the structure evolution from vertical to lamellar in the whole area. More areas become lamellar, better conducting network can be formed, which is supposed to be very suitable for EMI applications. The EMI SE in the X band of 8.2–12.4 GHz of the three kinds of GAs with the same thickness of 2 mm are shown in Figure 5b. The value range of EMI SE increases from GA-T0 (24.27 dB–25.34 dB) to GA-T2 (39.77 dB–41.45 dB), then to GA-T4 (47.90 dB–50.83 dB). The approximate two times enhancement from GA-T0 to GA-T4 strongly demonstrates the importance of the lamellar structures on EMI SE. Note that the maximum EMI SE (50.83 dB at 12.4 GHz) of GA-T4 is very high comparing to the other graphene-based aerogels with about 2 mm thickness as shown in Table S2. The EMI SE of the GA-T4 with the thickness from 1mm to 3mm were measured and shown in Figure 5c. It can be observed that with the thickness increasing, the range of EMI SE increases from (26.82 dB–27.63 dB) to (47.90 dB–50.83 dB), then to (65.50 dB–68.75 dB). Figure 5d shows the densities

of GA-T0, GA-T2, and GA-T4, which are very important for the light weight EMI. The EMI specific shield effectiveness (SSE, defined as shielding effectiveness divided by density) and the absolute shielding effectiveness (SSE/t, defined as SSE divided by thickness) of all samples were calculated, which can be found in Figure S9a and S9b and Figure 5e and 5f, respectively. The highest SSE curve in Figure S9b belong to 3 mm GA-T4 with the range from 3639.0 to 3819.6 dB cm^3 g^{-1} The highest SSE/t curve in Figure 5f belongs to 1 mm GA-T4 with the range from 14894.7 to 15351.9 dB cm^2 g^{-1}, while the lowest curve belongs to 3 mm GA-T4 with the range from 12130.1 to 12731.4 dB cm^2 g^{-1}. the SER values is the main reason why the 1mm sample has the highest SSE/t curve, while the 3 mm sample has the lowest curve. The maximum SSE and SSE/t is very high comparing to the other graphene-based aerogels as shown in Table S2.

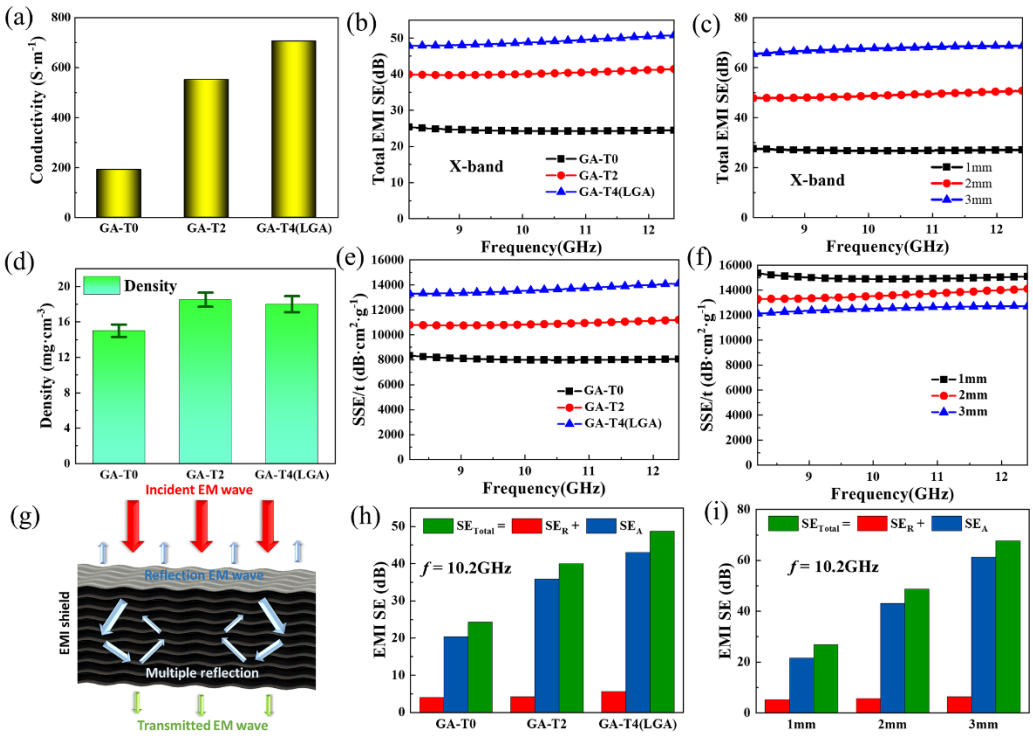

Figure 5. Electromagnetic interference (EMI) shielding of GAs. (a) Electrical conductivities of GA-T0, GA-T2, and GA-T4, respectively. EMI SE in X band of (b) GA-0, GA-T2, and GA-T4 with the thickness of 2 mm, and of (c) GA-T4 with the thickness from 1 mm to 3 mm. (d) Densities of GA-0, GA-T2, and GA-T4. Absolute EMI SE of (e) GA-T0, GA-T2, and GA-T4 with the thickness of 2 mm, and of (f) GA-T4 with the thickness from 1 mm to 3 mm. (g) Schematic diagram of electromagnetic shielding mechanism of the LGA structure. Contrast of

total shielding effectiveness (SE_{Total}), absorption shielding effectiveness (SE_A), and reflective shielding effectiveness (SE_R) at 10.2GHz of (h) GA-T0, GA-T2, and GA-T4 with the thickness of 2 mm, and of (i) GA-T4 with thickness from 1 mm to 3 mm, respectively.

The schematic diagram of the electromagnetic shielding mechanism in the LGA structure is depicted in Figure 5g. When the incident electromagnetic (EM) waves perpendicularly enter the LGA structure, the sublayers close to the upper surface of the structure mainly contribute to the reflection of the EM waves. When the EM waves enter the inside, they will be reflected and scattered circularly back and forth between the sublayers. Such multiple reflections and scattering processes promote the repeated EM energy dissipation (absorption), which leads to the significant attenuation of the incident EM waves.[35]. In order to better understand the EM shielding mechanism on the GAs, we have studied the relation between the total SE (SE_{Total}), absorption SE (SE_A) and reflective SE (SE_R) at 10.2 GHz in Figure 5h and 5i, where $SE_{Total} = SE_A + SE_R$. The SE_R is the small part of the SE_{Total} for each sample, and increases from 4.00 dB for GO-T0 to 4.20 dB for GA-T2, then to 5.67dB for GA-T4; while the SE_A is the main part in the SE_{Total}, and increases from 20.31 dB for GA-T0 to 35.84 dB for GA-T2, then to 43.07 dB for GA-T4. The improvement of the SE_A and SE_R is because GA-T4 with the LGA structure has higher conductivity as well as more free electrons on the sublayers. For the sublayers close to the surface, the free electrons mainly contribute to the improvement of the SE_R of the EM waves. For the inner sublayers of the sample, the free electrons will greatly improve the absorption effect due to the circular reflection. In Figure 5i, the increasing of SE_{Total} is also consistent with the curves in Figure 5c. With the thickness increasing, the SE_R increases from 5.24 dB to 5.67 dB, then to 6.38 dB, while the SE_A increases from 21.58 dB to 43.07 dB, then to 61.39 dB, which is due to the enhancement of the inner circularly reflection. Note that the SE_A increasing trend is linear when the thickness increases from 1 mm to 3 mm.

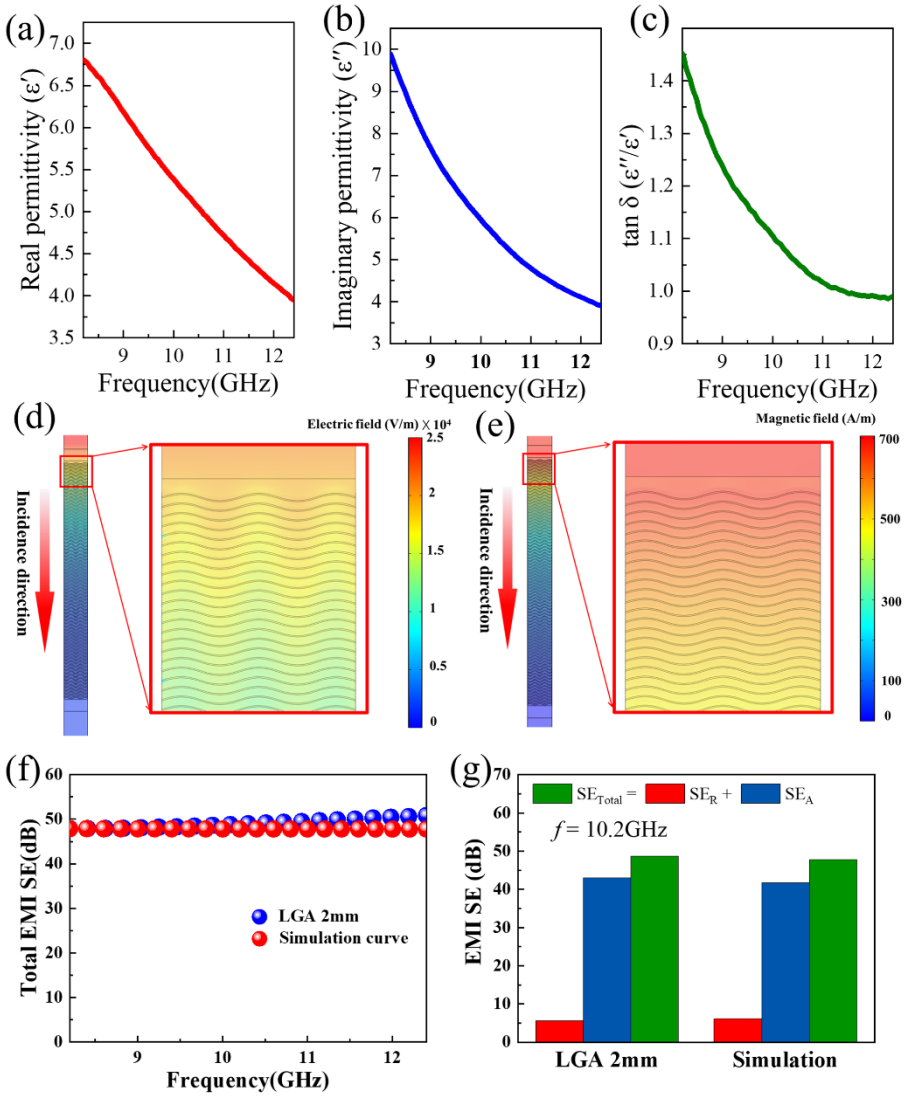

Figure 6. (a) Real and (b) imaginary parts of the complex permittivity, (c) dielectric loss tangent (tan δ = ε″/ε′) of LGA. Simulated (d) electric field and magnetic field distribution of LGA. (f) Simulated (red dots) and measured (blue dots) shielding performance of 2mm LGA. (g) Simulated total shielding effectiveness (SE_{Total}), absorption shielding effectiveness (SE_A), and reflective shielding effectiveness (SE_R) of LGA.

In order to further clarify the specific EMI shielding mechanism of LGA with the lamellar multi-arch structure, we tested the complex permittivity of the LGA and simulated the distribution of the LGA's electromagnetic field during the shielding process. Since there is no magnetism, the electromagnetic shielding behavior of LGA is attributed to its own dielectric loss (polarization loss and conduction loss). Therefore, the complex dielectric constant of LGA in the frequency range of 8.2 to 12.4 GHz was tested, as shown in Figure 6 a-c. Both of the Real dielectric constant (ε') And virtual permittivity (ε") are high, which is the reason of high EMI

SE. High ε′ value is mainly due to the strong polarization effect of LGA. A large number of side polar groups (-OH, -C=O, etc.) and rich defects in graphene sheets increase the number of polarization centers. ε″ is the sum of dielectric polarization and conductivity loss, high ε" is due to the increased conductivity of LGA with parallel arrangement and low porosity. Higher dielectric loss angle tangential (tanδ = ε″/ε′) reflects that EM wave dissipates more easily in the form of heat.[36]

Based on the measured complex dielectric constant and conductivity, the electromagnetic shielding behavior of LGA is simulated by COMSOL. The simulation model is based on the observed microscopic image (Figure S9), and is optimized into a parallel micro arch structure (Figure S14) for simplified calculation, and the structure is arranged periodically. Electromagnetic waves incident perpendicular to the LGA surface and the direction of polarization propagation parallel to the LGA surface. The decay trend of electromagnetic wave energy can be deduced from the distribution of electric field intensity (Figure 6d) and magnetic field intensity (Figure 6e). Along the incidence direction of the electromagnetic wave, the electric field intensity and magnetic field intensity inside the LGA gradually attenuate, which means that the electromagnetic wave is gradually absorbed along the vertical direction of the LGA. We speculate that this absorption is mainly due to the layered structure, which enhances the internal multiple reflection. Electromagnetic reflection generally occurs at the corresponding interface where the impedance mismatch occurs. The impedance mismatch between the layer of LGA and the air (Figure S13) and the higher layer density will result in enhanced multilayer reflection of the electromagnetic wave. In addition, the parallel arrangement of the layers facilitates the electron to absorb more electromagnetic energy and migrate through the intercalated channels, thus dissipating the electromagnetic energy as heat. On the other hand, near the surface of the sample, electromagnetic waves may escape through the graphene layer, so the reflected electromagnetic waves from these interfaces cannot be completely dispersed.[16, 37] Therefore, we believe that the construction of parallel layered networks has a significant impact on the EMI shielding performance of LGA. The simulated EMI SE results in Figure 5f-g show similar numerical values to the experimental data, verifying the accuracy of the modeling and simulation results.

2.5. Test and analysis of Piezoresistive Performance

The compressive properties of GA-T4 with the lamellar multi-arch structure was further studied. Figure 7a shows the stress-strain curves of the four compression cycles with strain amplitude of 20, 40, 60 and 80% in sequence for GA-T4. The sample size is 1×1 × 0.5 cm^3. The sample exhibits high compressibility with full recovery after large compression strain of 80% with the maximum compress stress of 166.51 kPa, which may be attributed to the micro-arch sublayers with the close packed graphene sheets. The compressive stress-strain curves of 1, 10 and 100 cycles for GA-T4 with compressive strain of 80% are shown in Figure 7b. Although there is energy dissipation after 10 compress-release cycles, the structure exhibits high fatigue resistance (the maximum compressive stress decreasing from 159.44 to 127.61 kPa) after 100 cycles and very small energy dissipation from 10 to 100 cycles. The SEM images of LGA after 100 cycles of compression as shown in Figure S16. Compared with the LGA structures before cyclic compression (Figure S9), the sublayers become flatter, and the small pores between lamellar structure are damaged and opened, which corresponds to the cyclic stress-strain curve (Fig. 7b). We suspect that the small hole and branched structure between lamellar structure are the reasons for the plastic deformation of LGA.

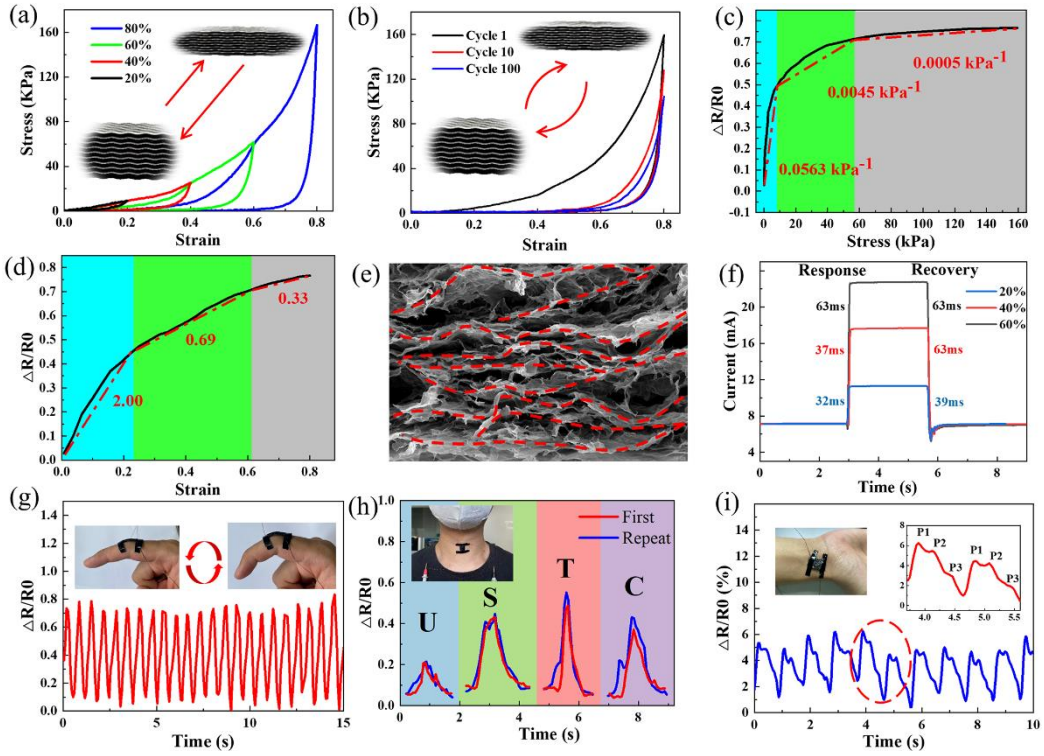

Figure 7. The compression properties and piezoresistive characteristics of GA-T4. Stress-strain curves (a) under different compression strains; (b) after 1, 10 and 100 cycles at 80% strain. The

calculated (c) pressure sensitivity and (d) Gauge factor (GF) from the plots of resistance variation ratios with respect to stress and strain, respectively. (e) SEM picture drawn with dashed lines to explain the piezoresistive sensing mechanism in LGA structure. (f) Response time and recovery time of the LGA-based pressure sensor under different compression strain. Real-time recording the resistance variation of (g) cycle bending-straightening of finger, (h) vocal cord vibration by speaking different letters of U, S, T and C, respectively, and (i) wrist pulse of an adult male.

The multi-arch LGA structure makes GA-T4 have great potential to be applied in piezoresistive sensors. To study the pressure-responsive properties of the LGA-based sensor, the resistance variation ratios ($\Delta R/R_0 = (R_0 - R_P)/R_0$; R_0 and R_P correspond to the resistance without and with stress, respectively) with respect to the stress and strain were measured. The pressure sensitivity (S) was calculated by the Equation $S = \delta(\Delta R/R_0)/\delta P$, where P represents the applied pressure (Figure 7c).[38] It can be observed that, when the stress in the range of 0.20 to 8.20 kPa, the S achieves 0.0563 kPa^{-1}. In the medium-pressure stage (8.20 - 56.97 kPa) , , the S is 0.0045 kPa^{-1}. For the stress larger than 56.96 kPa, the $\Delta R/R_0$ tends to be saturated and the S is only 0.0005 kPa^{-1}. Figure 7d shows the relation between the $\Delta R/R_0$ and strain. To evaluate the strain sensitivity, the Gauge factor (GF) was calculated by the Equation $GF = (\Delta R/R_0)/\varepsilon$, where ε is the applied strain[38]. For the strain in the range of 0 to 23%, the GF is 2.00, which is also a high sensitivity value. For the stain in the range of 23% to 61%, the GF decreases to 0.69. For the strain larger than 61%, the GF continues to decrease to 0.33. Figure 7e illustrates the SEM cross-section picture of the LGA structure of GA-T4. The dashed red lines were drawn as the possible electron transport routes, which are along the micro-arch lamellar structure. Combining with the sensitivity results in Figure 7c and 6d, when press the LGA-based sensor, the micro-arches will touch each other and result in the increase of the electron transport routes between each sublayer, which will greatly improve the conductivity.

In order to verify the practical applications of the LGA-based pressure sensor, a series of human behavior and physiological health tests were performed. As depicted in Figure 7f, LGA-based pressure sensor exhibits fast response time (32ms) and recovery time (39ms) at 20% strain. As shown in Figure 7g, the sensor can rapidly record the fast cycle bending-straightening

of the finger in real time. Each finger bending with an angle about 45° corresponds to one sharp peak in the curve. When then volunteer straightened finger, the resistance variation immediately dropped to a deep valley. The LGA-based pressure sensor also showed performance to detect much slighter mechanical signals. In Figure 7h, the pressure sensor was attached on the tester's throat. When the tester spoke the four different letters of U, S, T and C, respectively, the peaks with four different shapes appeared in the real-time resistance variation measurement, which recorded the small differences triggered by the vocal cord vibration. The peak shapes are generally well repeatable. The results show the great potential in the application of the aphasia research. It is worth noting that even the very subtle vibrations such as the wrist pulse can also be detected by the LGA-based pressure sensor as shown in Figure 7i. More importantly, the much finer vibration signals of the incoming blood wave (P1), ejected by the left ventricular wave (P2) and the reflected wave (P3) can be easily identified in the inset of Figure 7i. Compared to piezoresistive sensor with various samples reportedly (Table S3), our LGA based piezoresistive sensor has an advantage in the graphene aerogel based piezoresistive sensor, which indicates that our method has great effect on improving the performance of piezoresistive sensor. [39] However, compared with other composites, it still has room for improvement. Therefore, it is hopeful to obtain piezoresistive sensors with better performance by compounding materials with higher mechanical properties.

3. Conclusion

In summary, a 3D printing method of the multi-arch LGA structure is demonstrated. Two key solutions to overcome the challenges in this method are the design and preparation of an extrusion head to perform the uniform shear thinning stress on the GO sheets with a slit thickness of only 50 μm, and the maintenance of the orientation structure of the GO sheets by the ice-growth-inhibition of TBA on freezing substrate. It is the first time to demonstrate LGA structure by DIW method, which efficiently increase the scalable freedom of the structure shape and size. The LGA structure exhibits high electrical conductivity, electromagnetic interference (EMI) shielding efficiency (SE) and pressure sensitivity, which show great competitive advantages in the graphene-based aerogels. The LGA structure in this paper is an example for other 2D material-based aerogels, and many other unique properties and applications such as

thermal interface composites, oil removing absorbents, supercapacitors and battery cathode materials are waiting for exploration in future.

4. Experimental Section

Preparation of the Graphene Oxide (GO) dispersions for printing: Inks for printing were prepared by dispersing the initial GO water dispersion (1.0 wt%, purchased from Chengdu Institute of Organic Chemistry, Chinese Academy of Science) into mixed solvent of deionized water and tert-butyl alcohol (TBA) (Sinopharm Chemical Reagent Co., Ltd). The GO dispersions with TBA mass fractions of 0%, 20%, and 40% were marked as GO-T0 , GO-T2 and GO-T4, respectively. The GO concentrations of GO-T0, GO-T2 and GO-T4 are the same of 6 mg ml^{-1}, and the mean lateral size of the single-layer GO sheet was measured about 50 μm as shown in Figure S1.

Preparation of the slit extrusion heads: According to the different rheological properties of GO-T0, GO-T2 and GO-T4, the inside flow channel parameters of the slit extrusion heads were calculated and designed based on the coat-hanger die design equations. The inlet of the slit extrusion head was designed to match the outlet of a syringe without the needle head. A projection microstereolithography 3D printer (NanoArch S140, BMF Material Technology Inc) was used to print the designed slit extrusion heads. The fluid behavior of the GO dispersions in the designed extrusion head were simulated by COMSOL Mulitiphysics Software.

Preparation of Graphene Aerogels (GAs): Axxon VB-200 dispenser with three-axis motorized displacement stage, a gas pressure control system, and Five-axes manual displacement table was used to print the GO dispersions. The printing platform was refrigerated by a circulating cooling of ethanol cryovial to maintain the temperature at -40 °C. The prepared GO dispersion was printed layer by layer to the freezing substrate with the extrusion air pressure of 50 kPa. The moving speed of the extrusion head was 50 mm s^{-1}. Then, the printed frozen samples were freeze-dried in the lyophilizer (Scientz-12, Ningbo Scientz Biotechnology Co., LTD) at 1 Pa for 24 hours to obtain graphene oxide aerogels (GOAs). Next, the acid mixture of HI: HAC=1:2 was used for chemical reduction of the GOAs in a beaker at 40°C for 24 hours. The reduced samples were named as GA-T0, GA-T2, GA-T4 according to the mass fractions of TBA in the printed GO dispersions, respectively.

Preparation of Piezoresistive Pressure Sensor: The 5 mm thickness GA-T4 was cut into a cubic block with a size of 1cm × 1cm for the sensing performance tests. Then the cubic block GA-T4 was sandwiched by two ITO glasses and connected with the silver paste completely covered on the ITO conductive surface. Two copper wires connected two interfaces between the ITOs and the cubic block GA-T4 as the electrical measurement equipment.

Characterization: The microstructure and morphology of the prepared samples were recorded by FEI Quanta FEG 250 scanning electron microscope (SEM). The rheological properties of GO dispersions were measured by NETZSCH Instruments, Kinexus Lab+ rheometer. The birefringence behaviors of GO dispersions after extrusion were recorded by a polarized optical microscope (POM). The X-ray diffraction (XRD) patterns of the samples were measured by Bruker AXS GmbH, D8 Advance X-Ray diffractometer. The freezing points of the dispersions were measured by TA instrument, DSC250 differential scanning calorimeter. The chemical bonding structures of samples were measured by Thermo Fisher Scientific, Escalab 250Xi X-ray photoelectron spectroscopy (XPS). The chemical compositions of GO dispersions and graphene aerogels were measured by Horiba-JY, LABRAM HR Raman spectrometer. The electrical conductivities of the samples were measured by Suzhou Jingge Electronic Co. Ltd, ST-2258A four probe resistivity meter. The masses of the aerogels were measured by Shanghai Sunny Hengping Scientific Instrument Co., Ltd, FA2140 analytical balance. The sizes of the aerogels were measured by a digital caliper. The densities of the aerogels were calculated by dividing the mass by the corresponding volume. The mechanical and electrical properties of GA-T4 based pressure sensor was measured by Instron 3365 uniaxial testing machine and KEITHLEY2400 digital source meter, respectively. The electromagnetic interference shielding effectiveness (EMI SE) and electromagnetic parameters of the aerogels were measured by Keysight N5222A vector network analyzer in X band frequency ranging from 8.2 to 12.4 GHz.

Supporting Information

Supporting Information is available from the Wiley Online Library or from the author.

Acknowledgements

The authors gratefully acknowledge financial support by National Natural Science Foundation of China (No. 61575216), Key R&D programs in Jiangsu (No. BE2017082), R&D Plan for Key Areas of Guangdong Province (No. 2018B090905002) and Suzhou Science and Technology Program (No. SYG201850), Fundamental Research Funds for the Central Universities(NO.WK5290000002).

Hao Guo and Tianxiang Hua contributed equally to this work.

References

[1] M. Yang, N. Zhao, Y. Cui, W. Gao, Q. Zhao, C. Gao, H. Bai, T. Xie, *ACS Nano* **2017**, 11, 6817.

[2] Z.-H. Zhou, M.-Z. Li, H.-D. Huang, L. Li, B. Yang, D.-X. Yan, Z.-M. Li, *ACS Applied Materials & Interfaces* **2020**, 12, 18840.

[3] H. Duan, H. Zhu, J. Gao, D.-X. Yan, K. Dai, Y. Yang, G. Zhao, Y. Liu, Z.-M. Li, *Journal of Materials Chemistry A* **2020**, 8, 9146.

[4] K. Fu, Y. Yao, J. Dai, L. Hu, *Advanced Materials* **2017**, 29, 1603486.

[5] T. Liu, M. Huang, X. Li, C. Wang, C.-X. Gui, Z.-Z. Yu, *Carbon* **2016**, 100, 456.

[6] a) J. Zhao, D. Ma, C. Wang, Z. Guo, B. Zhang, J. Li, G. Nie, N. Xie, H. Zhang, *Nano Research* **2021**, 14, 897; b) X.-H. Li, X. Li, K.-N. Liao, P. Min, T. Liu, A. Dasari, Z.-Z. Yu, *ACS Applied Materials & Interfaces* **2016**, 8, 33230; c) Y. Dai, X. Wu, Z. Liu, H.-B. Zhang, Z.-Z. Yu, *Composites Part B: Engineering* **2020**, 200, 108263.

[7] a) A. K. Geim, *Science* **2009**, 324, 1530; b) K. S. Novoselov, A. K. Geim, S. V. Morozov, D. Jiang, Y. Zhang, S. V. Dubonos, I. V. Grigorieva, A. A. Firsov, *Science* **2004**, 306, 666; c) A. K. Geim, K. S. Novoselov, *Nature Materials* **2007**, 6, 183; d) A. A. Balandin, S. Ghosh, W. Bao, I. Calizo, D. Teweldebrhan, F. Miao, C. N. Lau, *Nano Letters* **2008**, 8, 902; e) C. Lee, X. Wei, J. W. Kysar, J. Hone, *Science* **2008**, 321, 385.

[8] J.-E. Kim, J.-H. Oh, M. Kotal, N. Koratkar, I.-K. Oh, *Nano Today* **2017**, 14, 100.

[9] Q. Wang, L. Xiang, D. Mei, Y. Xie, *International Journal of Thermophysics* **2020**, 41, 155.

[10] G. Shao, D. A. H. Hanaor, X. Shen, A. Gurlo, *Advanced Materials* **2020**, 32, 1907176.

[11] J. Han, G. Du, W. Gao, H. Bai, *Advanced Functional Materials* **2019**, 29, 1900412.

[12] P. Min, X. Li, P. Liu, J. Liu, X.-Q. Jia, X.-P. Li, Z.-Z. Yu, *Advanced Functional Materials* **2021**, 31.

[13] C. H. Wang, X. Chen, B. Wang, M. Huang, B. Wang, Y. Jiang, R. S. Ruoff, *Acs Nano* **2018**, 12, 5816.

[14] P. Liu, X. Li, P. Min, X. Chang, C. Shu, Y. Ding, Z.-Z. Yu, *Nano-Micro Letters* **2021**, 13.

[15] M. Panahi-Sarmad, M. Noroozi, M. Abrisham, S. Eghbalinia, F. Teimoury, A. R.

Bahramian, P. Dehghan, M. Sadri, V. Goodarzi, *ACS Applied Electronic Materials* **2020**, 2, 2318.

[16] W. Gao, N. Zhao, T. Yu, J. Xi, A. Mao, M. Yuan, H. Bai, C. Gao, *Carbon* **2020**, 157, 570.

[17] H.-Y. Mi, X. Jing, A. L. Politowicz, E. Chen, H.-X. Huang, L.-S. Turng, *Carbon* **2018**, 132, 199.

[18] P. Liu, X. Li, X. Chang, P. Min, C. Shu, Y. Li, Y. Kang, Z.-Z. Yu, *Carbon* **2021**, 178, 301.

[19] a) L. Onsager, *Annals of the New York Academy of Sciences* **1949**, 51, 627; b) R. Jalili, S. H. Aboutalebi, D. Esrafilzadeh, K. Konstantinov, J. M. Razal, S. E. Moulton, G. G. Wallace, *Mater. Horiz.* **2014**, 1, 87; c) S. Padmajan Sasikala, J. Lim, I. H. Kim, H. J. Jung, T. Yun, T. H. Han, S. O. Kim, *Chemical Society Reviews* **2018**, 47, 6013; d) S. Naficy, R. Jalili, S. H. Aboutalebi, R. A. Gorkin Iii, K. Konstantinov, P. C. Innis, G. M. Spinks, P. Poulin, G. G. Wallace, *Materials Horizons* **2014**, 1, 326; e) M. J. Abedin, T. D. Gamot, S. T. Martin, M. Ali, K. I. Hassan, M. S. Mirshekarloo, R. F. Tabor, M. J. Green, M. Majumder, *ACS Nano* **2019**, 13, 8957.

[20] P. Poulin, R. Jalili, W. Neri, F. Nallet, T. Divoux, A. Colin, S. H. Aboutalebi, G. Wallace, C. Zakri, *Proceedings of the National Academy of Sciences* **2016**, 113, 11088.

[21] G. Xin, T. Yao, H. Sun, S. M. Scott, D. Shao, G. Wang, J. Lian, *Science* **2015**, 349, 1083.

[22] C. Zhu, T. Liu, F. Qian, T. Y.-J. Han, E. B. Duoss, J. D. Kuntz, C. M. Spadaccini, M. A. Worsley, Y. Li, *Nano Letters* **2016**, 16, 3448.

[23] a) Z. Yu, T. Dai, S. Yuan, H. Zou, P. Liu, *ACS Applied Materials & Interfaces* **2020**, 12, 30990; b) L. Qian, H. Zhang, *Journal of Chemical Technology & Biotechnology* **2011**, 86, 172.

[24] a) J. Nemoto, T. Saito, A. Isogai, *ACS Applied Materials & Interfaces* **2015**, 7, 19809; b) Z. Lu, Z. Su, S. Song, Y. Zhao, S. Ma, M. Zhang, *Cellulose* **2018**, 25, 619.

[25] a) Y. Matsubara, *Polymer Engineering & Science* **1980**, 20, 716; b) A. Sullivan, A. Saigal, M. A. Zimmerman, *Polymers and Polymer Composites* **2021**, DOI: 10.1177/09673911211007019096739112110070190967391121100701 9; c) M. Kai, W. Xinhou, C. Qingguan, *Textile Research Journal* **2011**, 81, 1686; d) Q. Wu, H. Guo, T. Hua, L. Zhao, L. Li, B.

Qian, *RSC Advances* **2021**, 11, 15085.

[26] Y. Matsubara, *Polymer Engineering and Science* **1983**, 23, 17.

[27] X. Zheng, H. Lee, T. H. Weisgraber, M. Shusteff, J. DeOtte, E. B. Duoss, J. D. Kuntz, M. M. Biener, Q. Ge, J. A. Jackson, S. O. Kucheyev, N. X. Fang, C. M. Spadaccini, *Science* **2014**, 344, 1373.

[28] S. Al-Zangana, M. Iliut, M. Turner, A. Vijayaraghavan, I. Dierking, *2d Materials* **2017**, 4.

[29] a) D. Ying, Z. Wang, Y. Zheng, J. Cai, L. Zhang, *Macromolecular Rapid Communications* **2021**, 42, 2000502; b) K. Kasraian, P. P. DeLuca, *Pharmaceutical Research* **1995**, 12, 484.

[30] I. K. Moon, J. Lee, R. S. Ruoff, H. Lee, *Nature Communications* **2010**, 1, 73.

[31] L. J. Cote, F. Kim, J. Huang, *Journal of the American Chemical Society* **2009**, 131, 1043.

[32] a) B. Shen, D. Lu, W. Zhai, W. Zheng, *Journal of Materials Chemistry C* **2013**, 1, 50; b) Y. Zhou, Q. Bao, L. A. L. Tang, Y. Zhong, K. P. Loh, *Chemistry of Materials* **2009**, 21, 2950; c) N. Yousefi, M. M. Gudarzi, Q. Zheng, S. H. Aboutalebi, F. Sharif, J.-K. Kim, *Journal of Materials Chemistry* **2012**, 22, 12709.

[33] a) J. F. Shen, Y. Z. Hu, M. Shi, X. Lu, C. Qin, C. Li, M. X. Ye, *Chemistry of Materials* **2009**, 21, 3514; b) S. Das, S. Singh, V. Singh, D. Joung, J. M. Dowding, D. Reid, J. Anderson, L. Zhai, S. I. Khondaker, W. T. Self, *Particle & Particle Systems Characterization* **2013**, 30.

[34] a) J. Xi, Y. Li, E. Zhou, Y. Liu, W. Gao, Y. Guo, J. Ying, Z. Chen, G. Chen, C. Gao, *Carbon* **2018**, 135, 44; b) M. Mao, K.-X. Yu, C.-F. Cao, L.-X. Gong, G.-D. Zhang, L. Zhao, P. Song, J.-F. Gao, L.-C. Tang, *Chemical Engineering Journal* **2022**, 427, 131615.

[35] S. M. Zhao, Y. H. Yan, A. L. Gao, S. Zhao, J. Cui, G. F. Zhang, *Acs Applied Materials & Interfaces* **2018**, 10, 26723.

[36] a) X. Huang, G. Yu, Y. Zhang, M. Zhang, G. Shao, *Chemical Engineering Journal* **2021**, 426, 131894; b) M. Zhang, Z. Jiang, X. Lv, X. Zhang, Y. Zhang, J. Zhang, L. Zhang, C. Gong, *Journal of Physics D: Applied Physics* **2019**, 53, 02LT01; c) S. Bi, L. Zhang, C. Mu, H. Y. Lee, J. W. Cheah, E. K. Chua, K. Y. See, M. Liu, X. Hu, *Journal of Colloid and Interface Science* **2017**, 492, 112.

[37] S. Gupta, S. K. Sharma, D. Pradhan, N.-H. Tai, *Composites Part a-Applied Science and Manufacturing* **2019**, 123, 232.

[38] a) Z. Chen, H. Zhuo, Y. Hu, H. Lai, L. Liu, L. Zhong, X. Peng, *Advanced Functional Materials* **2020**, 30; b) Y. Qin, Q. Peng, Y. Ding, Z. Lin, C. Wang, Y. Li, J. Li, Y. Yuan, X. He, Y. Li, *Acs Nano* **2015**, 9, 8933.

[39] a) S.-W. Dai, Y.-L. Gu, L. Zhao, W. Zhang, C.-H. Gao, Y.-X. Wu, S.-C. Shen, C. Zhang, T.-T. Kong, Y.-T. Li, L.-X. Gong, G.-D. Zhang, L.-C. Tang, *Composites Part B: Engineering* **2021**, 225, 109243; b) S.-N. Li, Z.-R. Yu, B.-F. Guo, K.-Y. Guo, Y. Li, L.-X. Gong, L. Zhao, J. Bae, L.-C. Tang, *Nano Energy* **2021**, 90, 106502; c) J. Kuang, L. Liu, Y. Gao, D. Zhou, Z. Chen, B. Han, Z. Zhang, *Nanoscale* **2013**, 5, 12171; d) Y. Ding, T. Xu, O. Onyilagha, H. Fong, Z. Zhu, *ACS Applied Materials & Interfaces* **2019**, 11, 6685.